



Dry Reforming of Methane over Mn-modified Ni-based Catalysts

Alua M. Manabayeva^{1,2,4} · Päivi Mäki-Arvela² · Zuzana Vajglová² · Mark Martinez-Klimov² · Olha Yevdokimova² · Anssi Peuronen³ · Mika Lastusaari³ · Teija Tirri² · Tolkyn S. Baizhumanova^{4,5} · Kaisar Kassymkan⁴ · Gulnar N. Kaumenova⁴ · Alexandr R. Brodskiy⁴ · Rabiga O. Sarsenova⁴ · Kamshat A. Shorayeva⁴ · Dmitry Yu. Murzin^{2,4} · Svetlana A. Tungatarova^{4,5}

Received: 20 February 2024 / Accepted: 4 April 2024
© The Author(s) 2024

Abstract

Ni-based bi- and trimetallic Mn, Mg and aluminum containing catalysts prepared by the solution combustion synthesis (SCS) method were tested in dry reforming of methane (DRM). As a comparison 12 wt.% Ni/ α -Al₂O₃ catalyst prepared by wet impregnation was also investigated. The catalysts were characterized by means of XRD, N₂ physisorption, H₂-TPR, CO₂-TPD, NH₃-TPD, TPO, CHNS, TGA, SEM and TEM. Formation of crystalline MnAl₂O₄ was observed at high temperatures during SCS. The average nickel particle size varied in the range of 12–36 nm. Addition of Mn promoted reduction of Ni and elevated the amount and strength of the basic sites.

Keywords Methane Dry Reforming · Solution Combustion Synthesis · Mn Containing Catalysts · Syngas

1 Introduction

The emissions of methane and carbon dioxide produced from fossil fuels cause global warming in the world. Past decades the solutions of this problem have been found. It is important to avoid or minimize the fossil fuel treatment and include biogas production. Biogas is available and can be generated in anaerobic digester from biomass, agricultural and industrial wastes [1]. For example, biogas constitution from cow wastes is as follows: CH₄ (54.9 vol.%), CO₂ (39 vol.%), N₂ (5 vol.%), O₂ (0.9 vol.%), H₂S (400–1000 ppm_v) and NH₃ (30–53 ppm_v) [2].

Valuable constituents of biogas CH₄ and CO₂ are used to produce synthesis gas in dry reforming of methane process (DRM). This process is highly endothermic and includes two reactions (CO disproportionation and methane cracking), which forms carbon. The catalysts should be selected properly. Noble metals are highly active and resistant to coke deposition, however, due to their high costs non-noble metals (Ni, Co) are usually used [3].

However, Ni catalysts mostly are not resistant to carbon deposition. To improve catalyst stability the size nickel particles should be decreased, or strong interactions of the metal and the support can be implemented by adding promoters improving thereby stability [4]. The following supports, alumina [5], ceria and zirconia [6], magnesia [7], manganese oxide [8, 9] were reported to be suitable for nickel and lead to strong metal-support interactions. Moreover, cerium, magnesium and manganese can be used as promoters to improve CO₂ adsorption on the catalyst surface, minimizing the coke deposition.

The Ni-Mn catalyst supported on MgO-ZrO₂ displayed strong carbon formation (more than 2 mg/g·h) combined with a decrease of conversion [6]. Analogously, large coking was observed on Ni-Mn/Al₂O₃ in DRM [10]. On the contrary, addition of Mn to Ni/Al₂O₃ reduced significantly coke deposition and only a small decrease in catalytic activity was observed [11].

✉ Alua M. Manabayeva
manabaeva_2018@mail.ru

✉ Dmitry Yu. Murzin
dmurzin@abo.fi

¹ Kazakh-British Technical University, Almaty, Kazakhstan

² Laboratory of Industrial Chemistry and Reaction Engineering, Åbo Akademi University, Turku/Åbo, Finland

³ Department of Chemistry, University of Turku, 20014 Turku, Finland

⁴ D.V. Sokolsky Institute of Fuel, Catalysis and Electrochemistry, Almaty, Kazakhstan

⁵ Al-Farabi Kazakh National University, Almaty, Kazakhstan

The use of Mn_xO_y as a support or as an additive in ternary metal oxides is claimed to promote dispersion of nickel species enhancing at the same time catalyst stability [12]. In another study 10 wt.% Mn was incorporated onto the support. The conversion of CH_4 and CO_2 was 79.2% and 85.6%, respectively for Ni-Mn/Ce50-Zr50 catalyst, which was higher than for the catalyst without Mn [13].

The aim of this work was to demonstrate for the first time activity and stability of manganese promoted Ni–Al catalysts, prepared by the solution combustion method in dry methane reforming. The performance of the catalysts with time on stream of 30–40 min at each temperature was investigated and the long-term stability of catalysts was also investigated. The main purpose of Mn promotion was to elevate the carbon-resistance and long-term durability. For comparison, systems without catalyst were also investigated. Several different physicochemical methods, including X-ray diffraction (XRD), transmission electron microscopy (TEM), temperature-programmed techniques, scanning electron microscopy with elemental analysis (SEM–EDX), CHNS analysis were used to characterize catalysts and study coke formation of the spent catalysts.

2 Experimental Section

2.1 Preparation of the Catalysts

The catalysts were obtained by the solution combustion synthesis (SCS) method. Salts of metals $Ni(NO_3)_2 \cdot 6H_2O$ (Sigma Aldrich, 97%), $Mn(NO_3)_2 \cdot 6H_2O$ (Sigma Aldrich, 99%), $Al(NO_3)_3 \cdot 9H_2O$ (Carlo Erba, 99%) and urea (Sigma Aldrich, 99.5%) were weighted in the following quantities 3 g, 3 g and 4 g and 10 g, respectively. This mixture was dissolved in preheated to 80 °C 30 mL deionized water and thoroughly stirred until a solution becomes homogeneous. Thereafter, the beaker with the solution was placed in a muffle furnace preheated to 500 °C. The solution was burnt for 10–15 min. The same way of preparation was used for 15Ni-15Mn-20 Mg. Instead of $Al(NO_3)_3 \cdot 9H_2O$, $Mg(NO_3)_2 \cdot 6H_2O$ (Sigma Aldrich, 99.9%) was used. Finally, the powdered catalyst 15Ni-15Mn-20Al was cooled to room temperature in a fume hood. The catalysts with the following compositions were also obtained via the SCS: 15Ni-35Mn, 15Ni-15Mn-20 Mg.

2.2 Characterization of the Catalysts

The phase composition of as-prepared samples was investigated using X-ray diffraction (XRD). XRD patterns were obtained with a DRON-4–0.7 diffractometer with $CoK\alpha$ radiation with the wave number of 1.78892 nm in the range

of $2\theta = 5–100^\circ$. The phase analysis was carried out using HighScore Plus software and the PDF-4 + database [14, 15].

Temperature programmed reduction (H_2 -TPR), desorption using ammonia and carbon dioxide (NH_3 -TPD, CO_2 -TPD) and oxidation (O_2 -TPO) were done with MicrotracBelcat II instrument in a quartz tube reactor supplied with a thermal conductivity detector (TCD). The reduction was performed as follows: ca. 100 mg of the catalyst underwent pre-treatment at 200 °C for 2 h in flowing argon. After cooling down to 50 °C, the catalyst was flushed under flow of 5 vol.% H_2 (1.5 mL/min) and 95 vol.% Ar (28.5 mL/min). The temperature was increased to 800 °C with the rate of 10 °C/min holding at the target temperature for 20 min.

During O_2 -TPO measurements the catalyst (ca. 50 mg) was pre-treated at 300 °C for 2 h. After the catalyst sample was cooled to 50 °C, the temperature was increased to 865 °C with a rate of 10 °C/min under mixture of 5 vol.% O_2 (1.5 mL/min) and 95 vol.% Ar (28.5 mL/min). The target temperature was hold for 20 min. The equipment was connected to the mass spectrometer (OmniStar, Pfeiffer) facilitating evaluation of CO and CO_2 concentrations, from which the quantity of burnt carbon was quantitatively determined.

During NH_3 -TPD experiments, ca. 60–100 mg catalyst sample was pre-treated at 500 °C for 1 h. Then, the sample was cooled down to 50 °C, and ammonia went through preadsorption at 100 °C for 30 min. Physisorbed NH_3 was removed from surface of the catalyst for 1 h under flowing He. In the next step, the sample was heated up to 600 °C with a rate of 10 °C/min under the mixture of 5 vol.% NH_3 (1.5 mL/min) and 95 vol.% He (28.5 mL/min). The target temperature was kept for 20 min.

To estimate the quantity of carbon formed in the spent catalysts, a Thermo Fisher Scientific Flash 2000 Organic Elemental Analyzer equipped with a TC was used. This instrument was applied for defining carbon, hydrogen, nitrogen, and sulfur (CHNS) on the catalyst surface at the temperature of 950 °C in two columns. The samples were oxidized and reduced, thereafter, they were dried to purge the traces of humidity. Cystine, 2,5-bis(5-tert-butyl-benzoxazol-2-yl) thiophene, sulphanilimide and methionine were used as the standards for estimation.

Elemental analysis was measured by scanning electron microscopy (SEM) exhibited using a Zeiss Leo Gemini 1530 Scanning Electron Microscope combined with a Thermo Scientific UltraDry Silicon Drift Detector (SDD).

Estimation of coke deposits was done by thermogravimetric (TGA) and differential thermal analysis (DTA) of the used catalysts using an SDT Q600 equipment (TA techniques) under inert (N_2 or air) medium with a flow rate of 100 mL/min at 800 °C with the heating rate of 10 °C/min.

Textural features of the catalysts were defined by liquid N_2 physisorption on a Micromeritics 3Flex-3500 analyzer. Initially, the humidity was desorbed from the catalysts (ca.

0.15 g), followed by degassing for 20 h at 180 °C. After that, the samples underwent pre-treatment under vacuum at 180 °C for 5 h followed by differing relative pressures and adsorption of liquid N₂ at -196 °C. The pore size distribution was determined by DFT method, and the specific surface area was computed by BET method.

Transmission electron microscopic images and textural features were obtained using Jeol JEM-1400 Plus instrument supplied with 120 kV speeding-up voltage and 0.38 nm resolution and an OsisQuemesa 11 Mpix bottom-mounted digital camera. The catalysts underwent pre-treatment under H₂ stream (30–40 mL/min) at 450 °C for 2 h with heating rate of 10 °C/min. The gauging and computation of the metal particle sizes was performed using the ImageJ software.

2.3 DRM Experiments

DRM was carried out in fixed bed quartz reactor (5 mm ID, 20 mm length) under atmospheric pressure. 2 mL of the catalyst was put in the middle side of reactor and packed between glass wool and 4 mL quartz sand (2 mL in the bottom, 2 mL on the upper side). The gas hourly space velocity (GHSV) was 3000 h⁻¹ (100 mL/min). The reactants (33 mL/min CH₄ and 33 mL/min CO₂) were introduced together with the carrier gas (34 mL/min Ar). The product gas was analyzed every 15 min by achieving the nominal temperature. The temperature cycling tests were carried out at 600–900 °C by every 50 °C increment. After reaching 900 °C, the catalytic activity was checked at 600 °C again. The decrease of temperature followed by 1 min holding at 800 °C and 700 °C. The stability test was performed at 850 °C for 20 h. In stability experiments the temperature was risen from room to the nominal temperature. The temperature was kept at 650 °C for 2 min, followed by increasing to 750 °C and holding for 2 min. The holding time at 850 °C was in the range of 10–60 min (10 min for 30 min TOS, 60 min for 20 h TOS). For safety reasons stability tests were done for 7 h on the first day, 7 h on the second day and 6 h on the third day.

2.4 Gas Analysis

The starting reactants and reaction products were analyzed by Chromos GC-1000 chromatograph with Chromos software. The capillary column with FID was used to detect methane, carbon monoxide and carbon dioxide, whereas hydrogen, oxygen and nitrogen were analyzed by TCD using a packed column. The temperature of TCD was set to 200 °C, the column temperature was put at 40 °C, the evaporator temperature was 280 °C. As carrier gas, Ar with the gas velocity of 10 mL/min was used.

2.5 Calculations

The calculation of process parameters (CH₄ and CO₂ conversion – X, transformation rates calculated per mass of nickel – r, the space–time yield of hydrogen and carbon monoxide – STY and H₂/CO ratio) is demonstrated in Eq. (1–7). In the experiments, the error bar is X_{CH₄} = value ± 2.1%, X_{CO₂} = value ± 2.4%.

$$X_{\text{CH}_4} = \frac{(F_{\text{CH}_4,\text{in}} - F_{\text{CH}_4,\text{out}})}{F_{\text{CH}_4,\text{in}}} \times 100\% \quad (1)$$

$$X_{\text{CO}_2} = \frac{(F_{\text{CO}_2,\text{in}} - F_{\text{CO}_2,\text{out}})}{F_{\text{CO}_2,\text{in}}} \times 100\% \quad (2)$$

$$r_{\text{CH}_4} = \frac{F_{\text{CH}_4,\text{in}} - F_{\text{CH}_4,\text{out}}}{m_{\text{Ni}}} \quad (3)$$

$$r_{\text{CO}_2} = \frac{F_{\text{CO}_2,\text{in}} - F_{\text{CO}_2,\text{out}}}{m_{\text{Ni}}} \quad (4)$$

$$\text{STY}_{\text{H}_2} = \frac{F_{\text{H}_2,\text{out}}}{m_{\text{Ni}}} \quad (5)$$

$$\text{STY}_{\text{CO}} = \frac{F_{\text{CO},\text{out}}}{m_{\text{Ni}}} \quad (6)$$

$$\text{H}_2/\text{CO} = \frac{\text{STY}_{\text{H}_2}}{\text{STY}_{\text{CO}}} \quad (7)$$

F_i means a gas i molar flow.

The carbon balance (CB) was defined by Eq. (8) [16]:

$$\text{CB} = \frac{F_{\text{CH}_4,\text{out}} + F_{\text{CO}_2,\text{out}} + F_{\text{CO},\text{out}}}{F_{\text{CH}_4,\text{in}} + F_{\text{CO}_2,\text{in}}} \quad (8)$$

The Weisz-Prater parameter ϕ , was calculated using Eq. (9), taking into consideration the absence of external mass transfer limitations of the experiments of the current work.

$$\phi = \frac{r_{\text{obs}} r_p^2 RT}{p_{\text{CH}_4} D_{\text{eff}}} \leq 1 \quad (9)$$

where, r_p is the catalyst particle radius, r_{obs} is the observed reaction rate, p is the partial pressure of methane, D_{eff} is the effective diffusivity.

The following input data were considered for calculations: the binary diffusivity for reactants $D_{\text{AB}} = 1.69 \cdot 10^{-4}$ m²/s in accordance with the Chapman-Enskog equation [17], and Knudsen diffusivity $D_{\text{K}} = 4.46 \cdot 10^{-6}$ m²/s for

CH_4 in 15Ni-15Mn-20Al catalyst with the pore radius of 5.5 nm (defined by BJH method from N_2 physisorption). Thereafter, the effective diffusion coefficient was calculated from the Bosanquet equation to be D_e of $0.4 \cdot 10^{-6} \text{ m}^2/\text{s}$. Effective diffusivity was obtained from Eq. (10):

$$D_{\text{eff}} = \frac{\varepsilon}{\tau} D_e \quad (10)$$

with the value for porosity divided by tortuosity $\frac{\varepsilon}{\tau} = 0.1$. The value of $D_{\text{eff}} = 4.0 \cdot 10^{-7} \text{ m}^2/\text{s}$.

3 Results and Discussion

3.1 Characterization of Catalysts

3.1.1 Phase Composition

The recorded powder X-ray diffraction patterns are displayed in Fig. 1. Metallic Ni (henceforward Ni^0) [PDF 01-071-4655], which shows peaks at approximately 2θ of 52.5° , 61.4° and 92.4° , can be observed almost in all as-prepared and spent catalysts [18]. This demonstrates almost complete reduction of nickel oxide to metallic nickel in the catalyst

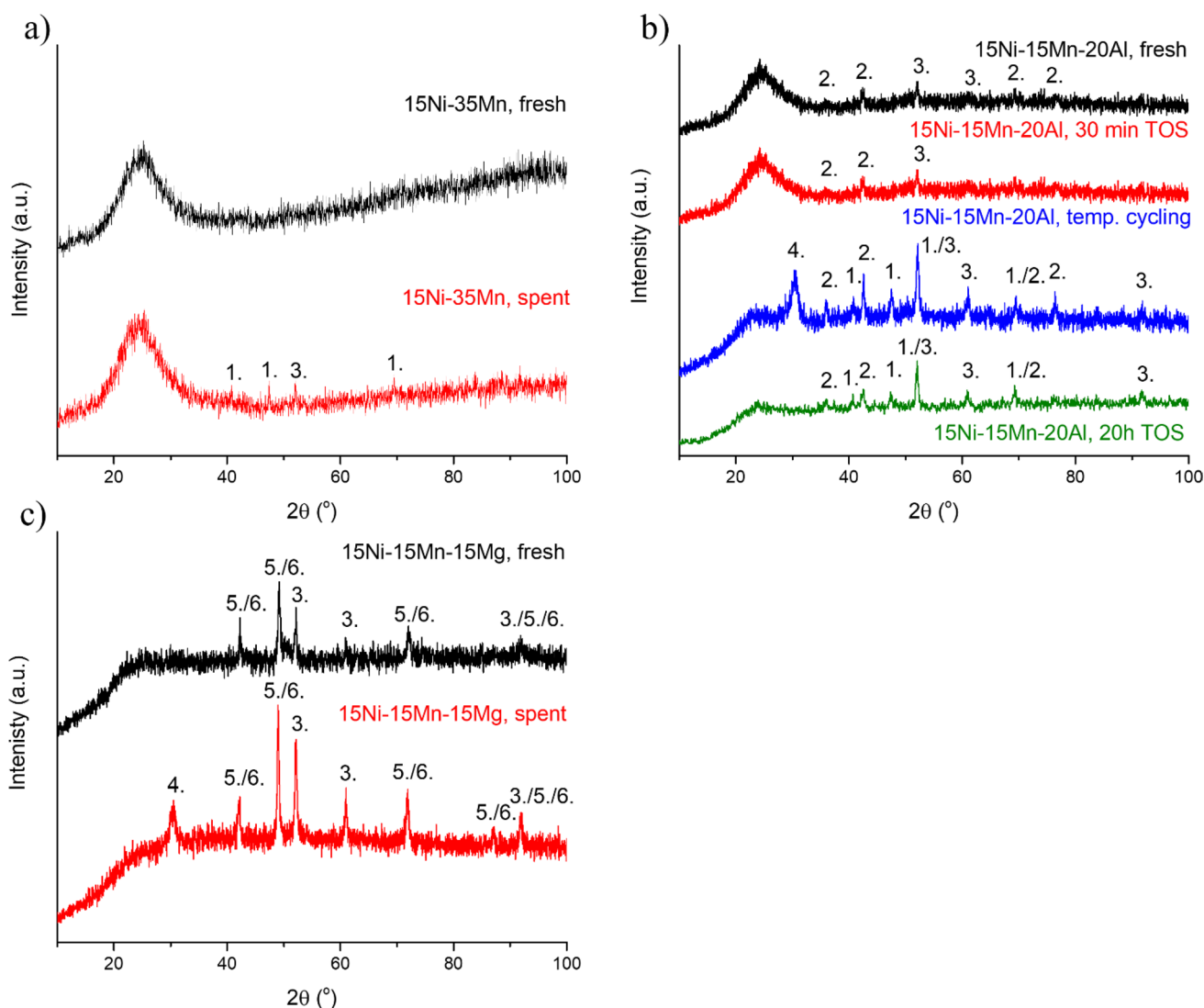
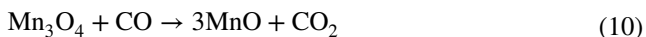


Fig. 1 X-ray diffraction patterns of **a)** 15Ni-35Mn, **b)** 15Ni-15Mn-20Al, **c)** 15Ni-15Mn-20 Mg. Notation: 1. MnO , 2. MnAl_2O_4 , 3. Ni^0 , 4. Mn_3O_4 , 5. $\text{Mn}_{0.5}\text{Ni}_{0.5}$ and 6. $\text{Mg}_{0.6}\text{Mn}_{0.4}$ (5. and 6. exemplify two of the several plausible halite structure phases comprised of a solid solution of MnO , MgO and NiO with potentially different relative ratios).

The spent catalysts (**a**, **b**) were used for 30 min at 850°C ; spent catalyst (**b**) was used for 20 h TOS; spent catalysts (**b**, **c**) were additionally used in the temperature range of $600\text{--}900^\circ\text{C}$ and back to 600°C ; conditions: $V_{\text{cat}} = 2 \text{ mL}$, $\text{GHSV} = 3000 \text{ h}^{-1}$, 100 mL/min

preparation [19, 20]. The diffraction peaks belonging to the nickel oxide phase were absent in all catalysts.

The bimetallic 15Ni-35Mn fresh catalyst exhibited a large amorphous feature and very low crystallinity (Fig. 1a) whereas, after DRM, very weak peaks corresponding most likely to MnO [PDF 04-007-3620] and Ni⁰ can be observed. On the other hand, in 15Ni-15Mn-20Al, the galaxite phase MnAl₂O₄ [PDF00-010-0310], with peaks at 2θ 35.6°, 42.1°, 68.5 and 75.6° [21, 22], was formed during preparation by the solution combustion method (Fig. 1b). Earlier reports demonstrated formation of the MnAl₂O₄ phase upon calcination at 850 °C [23]. There was virtually no detectable change of these peaks or the apparent amorphous feature in the spent catalyst after DRM. However, low crystallinity of both the fresh and spent catalysts means that PXRD provides very limited structural information in this case. After a temperature cycling experiment, crystallinity of the catalyst and the Ni⁰ phase increased, while peaks of two additional phases emerged corresponding to MnO and Mn₃O₄ [PDF 03-065-2776]. The presence of MnO can be explained by reduction of Mn₃O₄ in the presence of CO above 500 °C [24] as follows:



Analysis of 15Ni-15Mn-20 Mg shown in Fig. 1c, illustrates the likely formation of solid solutions consisting of oxides of Mn, Mg and Ni with the halite structure. The relative peak intensities and positions (at 2θ ca. 42.2°, 49.1° and 72.0°) can be interpreted as a set of different solid solution phases, for example, Mn_{0.5}Ni_{0.5}O [PDF 04-015-1624] and Mg_{0.6}Mn_{0.4}O [PDF 01-077-2379] as both have very similar lattice parameters (*a* = 4.294 and 4.319 Å, respectively). The corresponding diffraction peaks are present in both the fresh and the spent samples with roughly the same relative intensities. According to the previous literature [25], solid solutions of NiO and MgO both exhibiting the halite structures and similar lattice parameters (*a* = 4.178 and 4.212 Å, respectively) tend to diminish metal sintering. It is, therefore, noteworthy that solid solutions can be formed during preparation of catalysts by SCS and combustion methods [25, 26]. A more in-depth analysis of the nature of the solid

solution phases would require higher quality PXRD data as well as crystallite elemental mapping. In addition to the discussed solid solution phases, peaks of Ni⁰ with relatively narrow widths, indicating a large crystallite size, can be observed in both the fresh and spent catalyst materials. A comparison of the diffraction patterns of the fresh and the spent catalysts show that only one additional peak is found in the latter. The position of this peak fits the Mn₃O₄ phase, which was also observed in the 15Ni-15Mn-20Al catalyst after the temperature cycling experiment as described above.

3.1.2 Elemental Composition

The Energy Dispersive X-Ray Analysis results of the fresh catalysts (Table 1) demonstrate that the Ni/Mn weight ratio of 15Ni-15Mn-20Al was 0.9, while this ratio was much lower for bimetallic 15Ni-35Mn. For trimetallic 15Ni-15Mn-20 Mg the Ni/Mn weight ratio was 0.42 and its nickel content was thus lower in comparison to 15Ni-15Mn-20Al.

3.1.3 Metal Particle Size Defined by TEM

TEM analysis was performed to determine the average metal particle size (Fig. 2, Table 2) for the fresh (reduced). Figure 2a, b illustrates that for the fresh, reduced catalysts it was very difficult to identify nickel particles, because of the poor contrast, subsequently only for a few catalysts the nickel particle sizes are reported in Table 2.

3.1.4 Porosity and Surface Area

Textural properties of the fresh catalysts were determined by nitrogen physisorption demonstrating low surface areas (Table 2).

It was reported that the surface areas differ depending on type of fuel, therefore the surface area of the catalysts prepared by the solution combustion method can vary in the range of 49–153 m²/g for different fuels [27]. Some catalysts typically have low surface areas from 8 to 10 m²/g using glycine as a fuel [28]. In the case of urea, the surface area of Ni-based catalyst was also low, being 9 – 20 m²/g [29].

Table 1 Elemental composition of the fresh catalysts. In parenthesis the molar ratio of metals is given

Catalyst	Ni (wt.%)	M ^a (wt.%)	Al (wt.%)	O (wt%)	Ni/M	Ni/Al	M/Al
15Ni-15Mn-20Al (f)	24.66 ± 0.23	28.99 ± 0.18	11.01 ± 0.07	26.88 ± 0.13	0.9 (0.8)	2.2 (1.0)	2.6 (1.29)
15Ni-35Mn (f)	19.31 ± 0.23	65.14 ± 0.26	0.2 ± 0.03	15.35 ± 0.14	0.29 (0.28)	n.a	n.a
15Ni-15Mn-20 Mg	26.24 ± 0.30	15.47 ± 0.11 (Mg)	36.50 ± 0.24 ^b (Mn)	21.25 ± 0.23	1.7 ^c (0.70) (Ni/Mg)	0.42 ^d (0.66) (Ni/Mn)	n.a

^aM = Mn, Mg, ^bMn content, ^c Ni/Mg ratio, ^d Ni/Mn ratio

Fig. 2 TEM micrographs of the fresh catalysts **a)** 15Ni-15Mn-20Al, **b)** 15Ni-35Mn

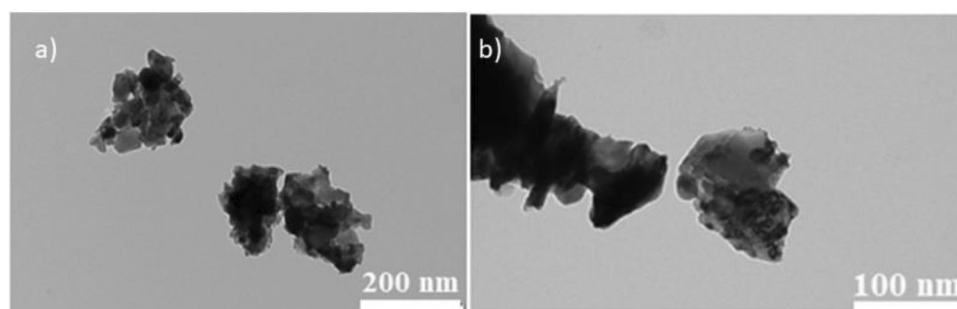


Table 2 Comparison of different fresh catalysts by several physico-chemical methods

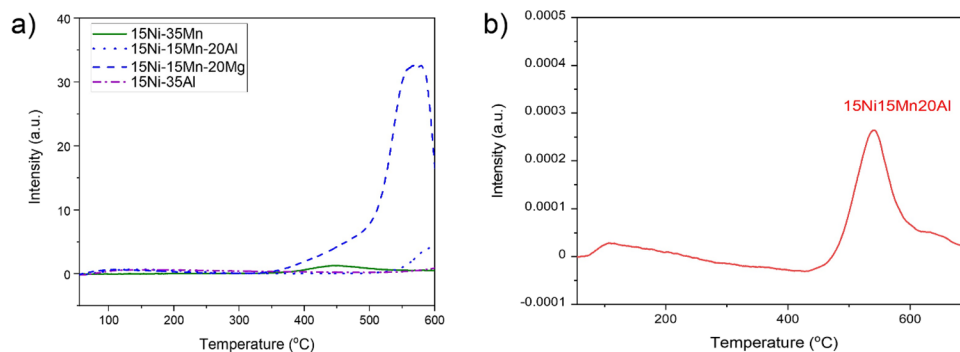
Catalyst	Surface area (m ² /g)	Pore volume (cm ³ /g)	Average metal particle size, nm (nm)
15Ni-15Mn-20Al	11	0.014	15
15Ni-15Mn-20 Mg	n.a	n.a	n.a
15Ni-35Mn	<4	0.002	11
15Ni-35Al [30]	n.d	n.d	13
12 wt% Ni/ α -Al ₂ O ₃ [31]	10	0.014	9

Basicity of 15Ni-15Mn-20Al was quite low (Fig. 3b, Table 4), while it was nearly twice as high for Ni-Mn/ γ -Al₂O₃ catalyst exhibiting 1:1 molar ratio of Ni to Mn as compared to Ni/ γ -Al₂O₃ [32].

3.1.6 Reducibility of the Catalysts Determined by Hydrogen TPR

TPR patterns of the Ni-based catalysts are depicted in Fig. 4. The TPR peak in the temperature range of

Fig. 3 **a** Acidity of various catalysts by NH₃TPD; **b** basicity of 15Ni-15Mn-20Al catalyst by CO₂ TPD



15Ni-35Al [30] and 12 wt% Ni/ α -Al₂O₃ [31] exhibited low surface areas in comparison with 15Ni-15Mn-20Al.

3.1.5 Acidity and Basicity of Catalysts Determined by Ammonia and CO₂ TPD

Acidity of different catalysts determined by ammonia TPD for 15Ni-15Mn-20Al and 15Ni-35Al was very low (Fig. 3a, Table 3).

Addition of Mn typically decreases acidity, for example in NiMn/ γ -Al₂O₃ in comparison to Ni/ γ -Al₂O₃ [32]. On the other hand, the current results are in accordance with [33], when acidity was the lowest for 40% MnO/ γ -Al₂O₃, being the highest for 10 wt.% MnO/ γ -Al₂O₃. In the current case, acidity of 15Ni-35Mn with the Mn content of 65 wt.%, was 50-fold that of the acidity of 15Ni-15Mn-20Al with the Mn content of 36 wt.% (Table 3 and Table 1).

Table 3 Temperature peaks and normalized area from ammonia TPD

Catalyst	T _{1,max} (°C)	T _{2,max} (°C)	T _{3,max} (°C)	Normalized area
15Ni-35Al [30]	140	n.a	n.a	0.01
15Ni-15Mn-20Al	136	600	n.a	0.002
15Ni-35Mn	450	n.a	n.a	0.08
15Ni-15Mn-20 Mg	565	n.a	n.a	1

Table 4 Temperature peaks for maximum desorption and normalized area from CO₂ TPD

Catalyst	T _{1,max} (°C)	T _{2,max} (°C)	T _{3,max} (°C)	Normalized area
15Ni-15Mn-20Al	105	540	n.a	0.29
15Ni-35Mn	Very small	0	0	0

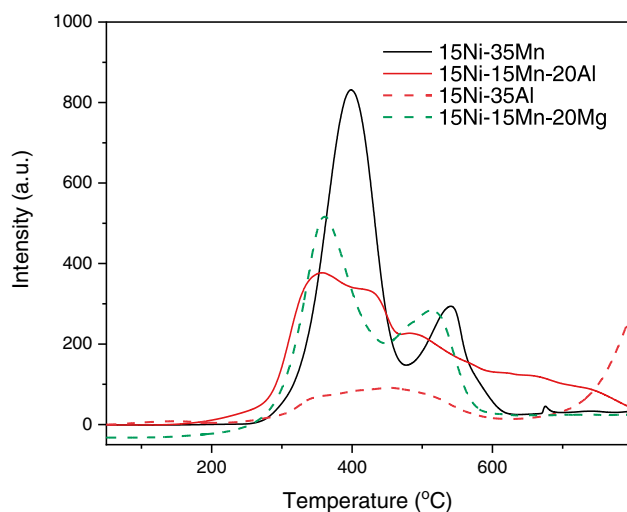


Fig. 4 Reducibility by H_2 -TPR of various Ni catalysts

400–500 °C can be explained by the reduction of NiO species strongly interacting with the support (15Ni-15Mn-20Al). It should be pointed out, however, that the presence of NiO crystallites was not observed in the current case in XRD.

The highest relative hydrogen consumption among the studied four Ni catalysts was obtained for 15Ni-15Mn-20Al indicating high reducibility of Ni and Mn species as well as an easy reduction of the metal species (Table 5). The TPR profile for 15Ni-15Mn-20Al shows a peak at 363 °C, which can originate both from NiO reduction or alternatively from reduction of Mn_2O_3 to Mn_3O_4 and the second peak at 475 °C from reduction of Mn_3O_4 to MnO. The corresponding peaks

Table 5 Temperature for maximum desorption of hydrogen and normalized peak area from hydrogen TPR

Catalyst	$T_{1,max}$ (°C)	$T_{2,max}$ (°C)	$T_{3,max}$ (°C)	Normalized area
15Ni-35Mn	399	542	n.a	0.98
15Ni-15Mn-20Al	363	475	n.a	1.0
15Ni-35Al [30]	306	384	800	0.30
15Ni-15Mn-20 Mg	360	508	n.a	0.97

Table 6 Results of catalytic performance at following conditions: $T=850$ °C, $CH_4:CO_2:Ar=1:1:1$, $GHSV=3000$ h^{-1} for TOS=30 min. Notation: r_{CH_4} , r_{CO_2} – rates of reactants transforma-

Catalyst	r_{CH_4} (mol/ g_{Ni}/s)	r_{CO_2} (mol/ g_{Ni}/s)	r_{CH_4}/r_{CO_2}	TOF_{CH_4} (s^{-1})	STY_{H_2} (mol/ g_{Ni}/s)	STY_{CO} (mol/ g_{Ni}/s)	CB (%)	Deactivation rate (%/min/ g_{cat}) ^a	H_2/CO
15Ni-35Mn	$3.1 \cdot 10^{-4}$	$3.1 \cdot 10^{-4}$	1.0	0.41	$6.1 \cdot 10^{-4}$	$4.8 \cdot 10^{-4}$	85	0.33	1.3
15Ni-15Mn-20Al	$2.1 \cdot 10^{-4}$	$1.7 \cdot 10^{-4}$	1.2	0.42	$3.8 \cdot 10^{-4}$	$2.4 \cdot 10^{-4}$	68	0.1	1.5
15Ni-35Al [30]	$0.75 \cdot 10^{-4}$	$0.70 \cdot 10^{-4}$	1.1	0.006	$1.5 \cdot 10^{-4}$	$1.0 \cdot 10^{-4}$	74	0.03	1.5

^aDeactivation rate is calculated during the decrease in CH_4 conversion per time and catalyst mass

were found at 377 °C and 452 °C, respectively in [34]. It is also important to note that reduction of NiO occurs at a lower temperature for Mn-promoted 15Ni-15Mn-20Al, than for 15Ni-35Al, and the amount of consumed hydrogen was lower for the latter catalyst with a higher Al-content. This result indicates strong interactions between Ni and the support. It was reported in [35], that hydrogen consumption was already started at 230 °C for 5Ni-15Mn/Al, while in the current case for 15Ni-15Mn-20Al it started at 180 °C. XRD results of the spent catalyst used in the reducing atmosphere during DRM in this work, demonstrate also the presence of MnO and Mn_3O_4 . For 15Ni-15Mn-20 Mg the presence of NiO-MnO solid solution determined by XRD, shifted the peak to lower temperatures. The reduction process consists of two steps: $MnO_2 \rightarrow Mn_3O_4 \rightarrow MnO$, where the hydrogen consumption in the first step (lower temperature peak) is higher than the second step (higher temperature peak) as indicated in [36].

3.2 Catalytic Results

3.2.1 Short-Term Catalytic Tests

Catalytic performance of different Ni-based catalysts was tested in DRM at 850 °C for TOS of 30 min with the results demonstrated in Tables 6 and 7. Literature data are summarized in Table 8. In all cases except 15Ni-35Mn catalyst the methane transformation rate was higher than CO_2 transformation rate. This catalyst exhibited initially also the highest methane transformation rate, having Ni particles of the optimum size, 22 nm. Furthermore, it can be seen from

tion, STY_{H_2} , STY_{CO} —space-time yields of products, CB – carbon balance, TOF_{CH_4} – initial turn over frequency of CH_4 , defined as moles converted methane divided by moles of metal and time

CHNS results, that a low amount of carbon was accumulated on 15Ni-35Mn catalyst.

Methane transformation rate could not be directly correlated with hydrogen TPR results (Fig. 5a). When, however, catalyst coking normalized by the nickel content was plotted as a function of methane transformation rate, coking was higher in case of the slower methane transformation rates (Fig. 5). When carbon formation in the spent catalyst was correlated with the amount of acid/basic sites available in the reactor, taking also into account that different catalyst mass was used keeping the catalyst volume constant, it can be seen that the methane transformation rate could not be correlated with either acidity or basicity (Fig. 5b).

For the second most active catalyst in methane transformation, 15Ni-15Mn-20Al (Table 6), a rather high carbon formation was obtained, although the available acid/basic sites in the reactor were low. The fresh reduced 15Ni-15Mn-20Al catalyst contained MnAl_2O_4 and metallic nickel. In the spent catalyst, however, the spinel phase was decomposed during DRM, and the catalyst exhibited a very low crystallinity (Fig. 1b). Furthermore, rather large metal particles were present in the spent 15Ni-15Mn-20Al based on TEM (Table 9). According to [17], addition of manganese can reduce the particle size of nickel. However, MnO itself as a support formed large nickel particles, probably due to its small surface area.

The highest initial methane transformation rate was observed with the Ni size of 21 nm for 15Ni-35Mn catalyst, while with larger Ni particles, lower reaction rates were recorded analogously to the data reported previously for steam reforming of methane (Fig. 6) [37].

Space–time yields of hydrogen and H_2 and CO followed the same order as methane transformation rate, indicating

that the highest STYs were obtained over 15Ni-35Mn catalyst and the lowest ones over 15Ni-35Al. The deactivation rate was clearly correlating with the methane transformation rate (Figs. 7, 8 and 9). 15Ni-15Mn-20Al catalyst gave the low carbon balance and low H_2 yields (Table 6; Figs. 8 and 9).

The highest deactivation was determined for 15Ni-35Mn, and even if over this catalyst no carbon nanofibers were formed (Fig. 10b), it still contained some carbon deposits (Table 8).

3.2.2 Effect of Temperature Cycling on Catalytic Performance

Based on the short-term DRM results, it was decided to investigate the effect of temperature cycling for 15Ni-15Mn-20Al catalyst, and as a comparison a trimetallic catalyst 15Ni-15 Mg-20Mn without Al was also investigated. The following stepwise temperature program was applied: temperature was initially at 600 °C for a certain time, after which it was stepwise increased by 50 °C up to 900 °C, thereafter switching back to 600 °C (Fig. 8, Table 7).

The initial methane transformation rate was higher for 15Ni-15 Mg-20Mn followed by 15Ni-15Mn-20Al. The Ni particle size for the spent 15Ni-15Mn-20Al was 25 nm. Furthermore, the rate for CO_2 transformation at a low temperature of 600 °C was slightly higher than that for methane for both catalysts, while at 800 °C the methane transformation rate was higher. Based on the methane transformation rates, the activation energy was determined for both catalysts (Table 7). The results showed that the activation energy for these catalysts in the lower temperature range was 45 kJ/mol, while at higher temperature activation energies were 21 kJ/mol for 15Ni-15Mn-20Al indicating that mass transfer

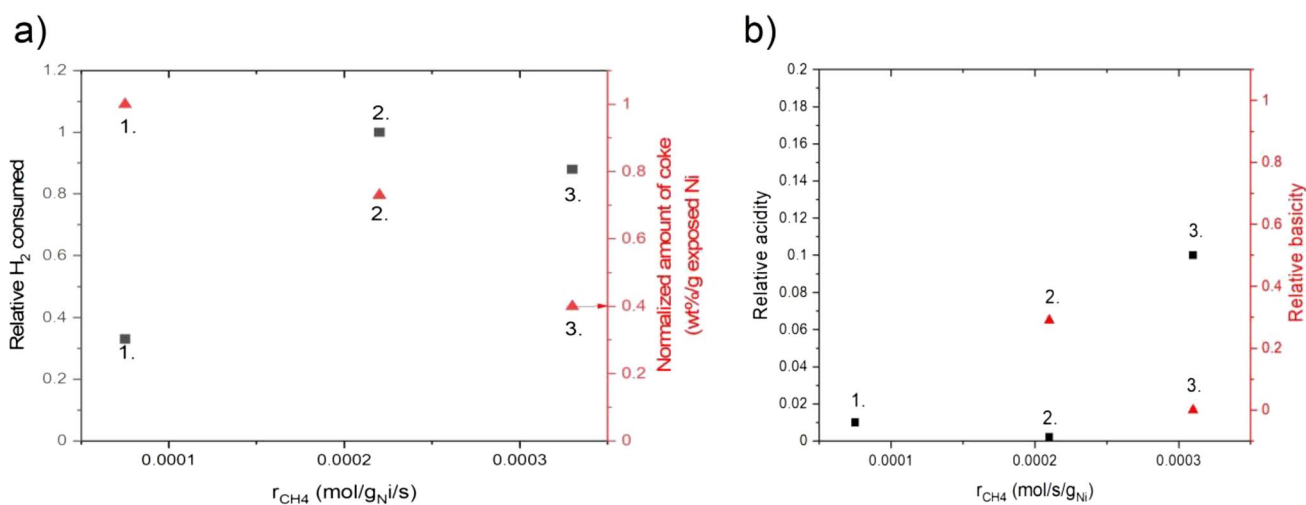


Fig. 5 Comparison of different physicochemical methods **a** relative hydrogen consumption in TPR (■) and carbon content defined by CHNS; **b** relative acidity (■)/basicity (▲) of the catalysts as a function

of CH_4 transformation rate. Conditions: CH_4 : CO_2 : Ar = 1:1:1, 850 °C, $\text{GHSV} = 3000 \text{ h}^{-1}$, $V_{\text{cat}} = 2 \text{ mL}$. Notation: 1. 15Ni-35Al, 2. 15Ni-15Mn-20Al, 3. 15Ni-35Mn

Table 7 Rate for CH₄ and CO₂ transformation, initial TOF for methane transformation and carbon balance (CB) at 600 °C initially and after temperature cycling at 600 °C (given in parenthesis) and rate for CH₄ and CO₂ transformations at 800 °C over various catalysts used in temperature cycling tests from 600–900 °C and back to 600 °C

Entry	Catalyst	$r_{\text{CH}_4+600}^{\text{oC}}$ (mol/g _{Ni} /s)	$r_{\text{CO}_2+600}^{\text{oC}}$ (mol/g _{Ni} /s)	TOF _{CH₄+600} (s ⁻¹)	CCB ₆₀₀ %	$r_{\text{CH}_4+800}^{\text{oC}}$ (mol/g _{Ni} /s)	$r_{\text{CO}_2+800}^{\text{oC}}$ (mol/g _{Ni} /s)	CB ₈₀₀ %	% C	STY _{H₂+800} ^{oC} (mol/g _{Ni} /s)	STY _{CO+800} ^{oC} (mol/g _{Ni} /s)	H ₂ /CO	E _A (kJ/mol)
1	15Ni-15Mn-20Al	5.1·10 ⁻⁵ (2.5 ⁻⁴)	6.6·10 ⁻⁵ (2.3·10 ⁻⁴)	Very low	694 (92)	2.1·10 ⁻⁴	1.8·10 ⁻⁴	79		3.3·10 ⁻⁴	2.7·10 ⁻⁴	1.2	45 (600–800) 21 (800–900)
3	15Ni-15Mn-20 Mg	3.2·10 ⁻⁵ (4.8·10 ⁻⁵)	3.8·10 ⁻⁵ (4.4·10 ⁻⁵)	0.11	794 (85)	8.4·10 ⁻⁵	8.3·10 ⁻⁵	67		1.2·10 ⁻⁴	1.1·10 ⁻⁴	1.1	36 (600–750) 4 (800–900)

limitations were present at high temperatures. The carbon balance after temperature cycling experiment was higher for the spent 15Ni-15Mn-20Al than for 15Ni-15Mn-20 Mg (Table 7), which is related to a very high acidity of the latter catalyst (Table 3).

Space-time yields calculated per mass of nickel for hydrogen and CO were also 2.8 and 2.5 fold higher for 15Ni-15Mn-20Al than for 15Ni-15Mn-20 Mg.

It has been reported that the small particle size is effective in inhibiting the carbon deposition [38]. Thus, in the current case large particles accelerated coke formation [39]. Ni sintering was not observed in all cases because the catalysts did not lose their activity, when returning to 600 °C.

3.2.3 Long Time Stability

The long-term stability for 20 h TOS was conducted over 15Ni-15Mn-20Al catalyst due to its higher activity. Between experiments, the reactor was cooled to room temperature and the experiment was continued in the following day due to safety reasons. The catalytic results are encouraging as no significant deactivation was observed during 20 h of time-on-stream (Fig. 9, Table 8) for 15Ni-15Mn-20Al. As a comparison, Ni-MnOx/MnAl₂O₄ catalyst [40] gave a low deactivation rate, calculated per converted CO₂ in DRM at 650 °C, namely 0.01%/(min·g_{cat.}). It was stated that for this catalyst with the molar ratio of Ni:Mn:Al of 1:1:6, deposited carbon was very reactive on the catalyst surface [40]. In the current case for 15Ni-15Mn-20Al the ratio of N:Mn:Al was 0.8:0.8:1 with the manganese content much lower in comparison to alumina present in the reference catalyst of [40].

NiAl catalysts were investigated in [41]. Among all catalysts, 14 wt.% Ni and 33 wt.% Ni (Table 8, entry 1) loaded catalysts exhibited high activity at 650 °C. However, in the stability test NiAl(15) was strongly deactivating during the first hours (results for NiAl(14) not shown in Table 8). NiAl(33) was stable for 100 h, thereafter the conversion values decreased by 10% after 100 h, however, the catalyst was stable until the end of the test [41]. Another good promoter is La, as 15 wt.% Ni-10 wt.% La/Fe-clay [42] demonstrated high stability during 5 h without any deactivation (Table 8, entry 2). Manganese oxide is an efficient promoter to suppress coke deposition in CO₂ reforming of methane (Table 8, entry 3) [23]. As Mn content increases, stability is improved accordingly. However, at a high Mn loading the activity decreased to some extent. Thus, there seems to be an optimum MnO loading (ca. 10 wt.%) that gives high stability without a significant compromise in activity. The carbon balance stayed constant at ca. 84%. The CO₂ transformation rate was 31% lower than the CH₄ transformation rate (Fig. 9a). The H₂/CO ratio was close to unity being 1.1–1.2. The methane and CO₂ conversions were stable, being 86–93% and 83–87%, respectively (Table 8). This result is better in

Table 8 Comparison of different catalysts used in DRM

Entry	Catalyst	Reaction conditions	X _{CH₄} (%)	X _{CO₂} (%)	H ₂ /CO	S _{BET} (m ² /g)	Metal particle size (nm)	TOS (h)	Ref
1	NiAl(33)	CH ₄ :CO ₂ :Ar = 10:10:80 (vol.%), 650 °C, flow rate = 1200 mL/min	^a 95 ^b 85	^a 85 ^b 75	^a 0.89 ^b 0.93	^a 54 ^b 59	^a 29	200	[41]
2	15 wt.% Ni-10 wt.% La/Fe-clay	CH ₄ :CO ₂ :Ar = 1:1:8, 750 °C, GHSV = 20,000 h ⁻¹	45	57	0.7	13	n.a	5	[42]
3	5 wt.% Ni-10 wt.% Mn/Al ₂ O ₃	CH ₄ :CO ₂ = 1:1, 650 °C, flow rate = 81 ML/μmol s	-	*r _{CO₂} = 270 μmol/g _{cat} s	n.a	99	16	25	[23]
4	15Ni-15Mn-20Al	CH ₄ :CO ₂ = 1:1, 650 °C, GHSV = 3000 h ⁻¹	91 91 ^c	87 75 ^c	1.1 1.1 ^c	<4	n.a	20	Current work
5	12 wt% Ni/α-Al ₂ O ₃	CH ₄ :CO ₂ :Ar = 1:1:1, 850 °C, GHSV = 3000 h ⁻¹	93	92	1.1	7	15	10	[31]

*r_{CO₂} denotes reaction rate by CO₂

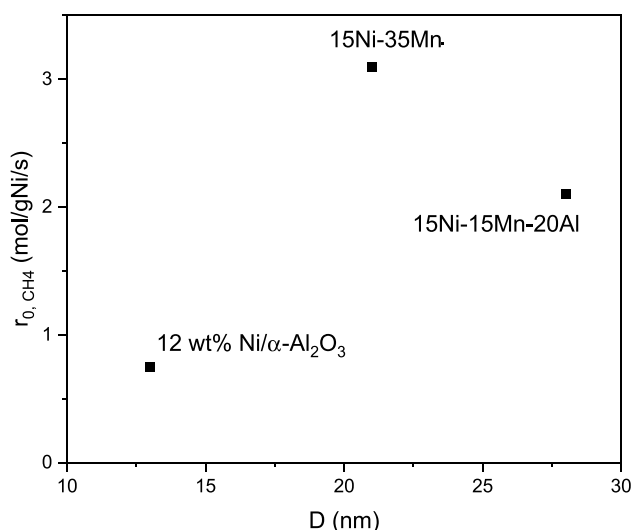
^a denotes initial value, ^b value after 200 h, ^c value after 20 h

n.a. not available

Table 9 Comparison of different spent catalysts by several physicochemical methods

Catalyst	Surface area (m ² /g)	Pore volume (cm ³ /g)	Average metal particle size (nm)	^a Normalized carbon (wt%/g _{Ni})	^a H/C molar ratio
15Ni-15Mn-20Al	<4	0.007	^a 28, ^b 25	0.75	0.63
15Ni-15Mn-20 Mg	n.a	n.a	^b 28	n.a	n.a
15Ni-35Mn	<4	0.003	^a 21	0.39	1.2
15Ni-35Al [30]	9	0.0014	12	1	0.26
12 wt% Ni/α-Al ₂ O ₃ [31]	7	0.011	^c 15	n.a	n.a

^a – 30 min TOS, ^b – temperature cycling, ^c – 10 h TOS

**Fig. 6** Initial CH₄ transformation rate as a function of the mean nickel particle size of the spent catalyst used in DRM at 850 °C for 30 min

comparison with the results presented in [43]. In the current work, the Ni/Mn molar ratio was 0.66 and the high DRM temperature of 850 °C was applied. In [43] it was stated that Ni/Mn ratio of 2 can afford a good catalytic activity. Despite a lower Ni/Mn ratio, STY_{CO} and conversion were almost not changing (Fig. 9b).

3.3 Characterization of the Spent Catalysts

3.3.1 Metal Particle Size of Spent Catalysts Defined by TEM

TEM analysis was performed to determine the average metal particle size (Fig. 10, Table 9) for the spent catalysts used in short-term DRM for 30 min at 850 °C and for the temperature cycling experiments.

For 15Ni-15Mn-20Al spent catalyst in temperature cycling the metal particles were small, however, also carbon nanotubes with the diameter of 13 nm were formed (Fig. 10b). Nickel particles were found at the tip of the

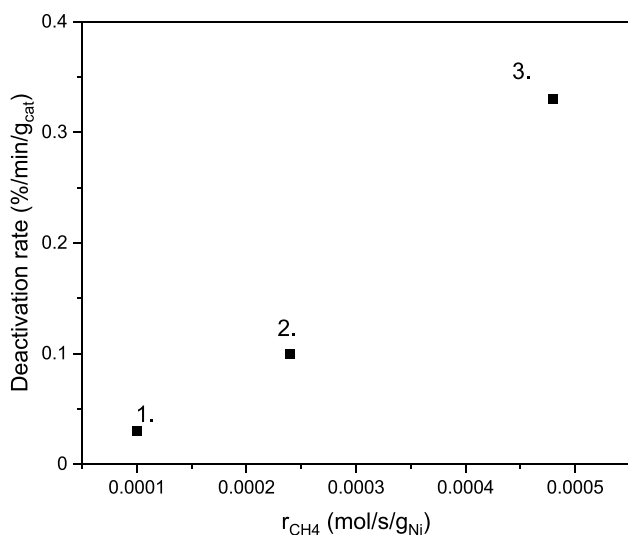


Fig. 7 The influence of methane transformation rate on the catalyst deactivation rate. Conditions: CH₄: CO₂: Ar=1:1:1, 850 °C, GHSV=3000 h⁻¹, V_{cat}=2 mL. Notation: 1. 15Ni-35Al, 2. 15Ni-15Mn-20Al, 3. 15Ni-15Mn-20Al

nanotubes resulting from formation of metallic nickel during DRM. At the same time crystallinity of the catalyst increased confirmed by XRD (Fig. 1b). Large Ni particles were observed in the spent 15Ni-15Mn-20Al and 15Ni-15Mn-20 Mg catalysts after the temperature cycling experiment (Table 9) indicating metal sintering (compare with Table 2).

Low carbon deposition has been reported for Mn-containing catalysts [40] because carbonaceous species can be reactive in these catalysts. It was reported in [44], the higher coke deposition was observed on the catalyst with larger metal particles. Location, quantity and the type of carbon are affected by the nickel dispersion [45]. Carbonaceous species oxidized in air at mild temperatures are of amorphous type. In the current case, the coke in Ni-Mn-Al burnt at high temperature, can be considered as the graphitic coke or coke filaments. Furthermore, 15Ni-15Mn-20Al exhibited the largest metal particle size after the experiment (Table 9), thus increasing the amount of carbon. In another work [46] activity of nickel

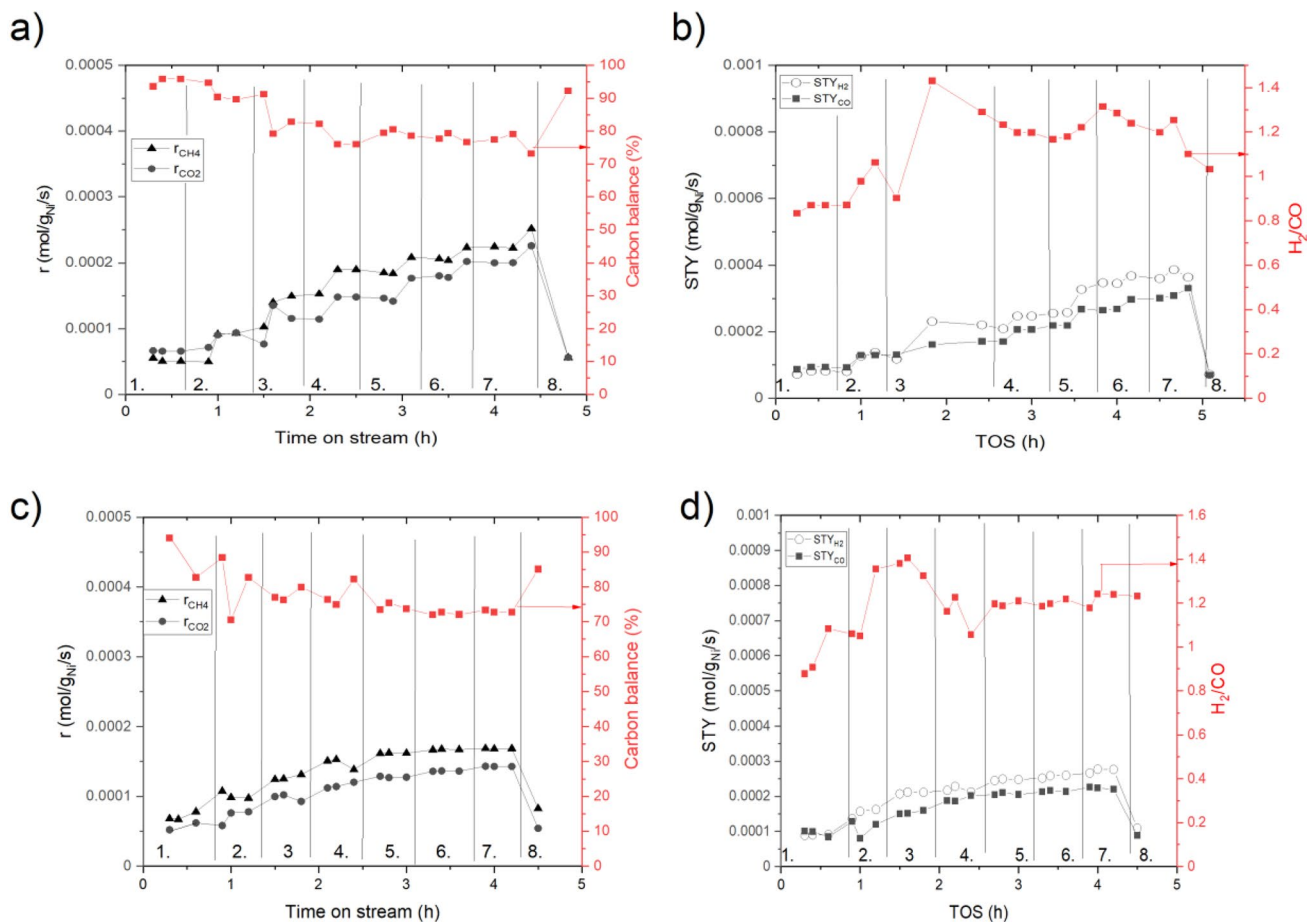


Fig. 8 a, c Rates for methane and CO₂ transformations and carbon balance, **b, d** space-time yields of H₂ and CO and H₂/CO ratio in DRM over **a, b** 15Ni-15Mn-20Al, **c, d** 15Ni-15 Mg-

20Mn at 600 – 900 °C and back to 600 °C. Conditions: V_{cat}=2 mL, GHSV=3000 h⁻¹. Notation: 1. 600 °C, 2. 650 °C, 3. 700 °C, 4. 750 °C, 5. 800 °C, 6. 850 °C, 7. 900 °C, 8. 600 °C

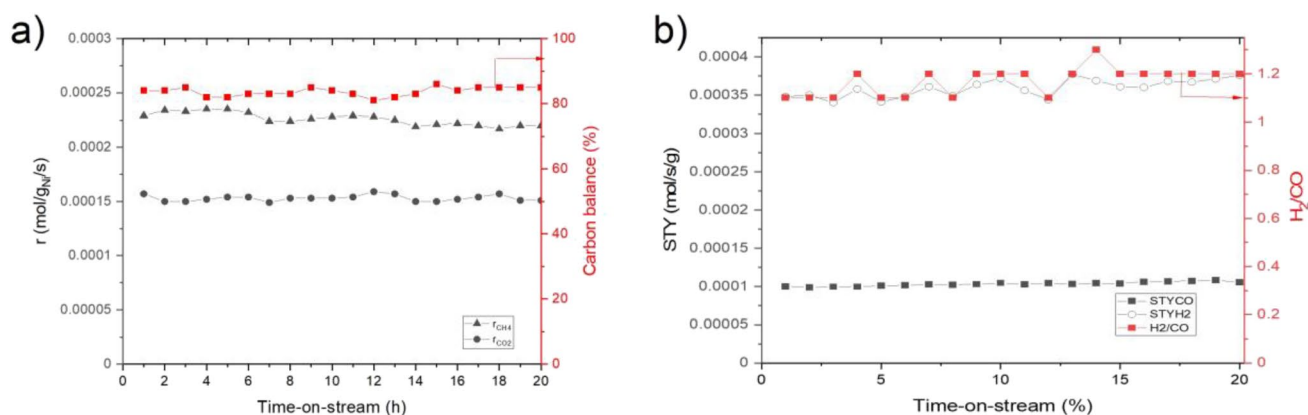
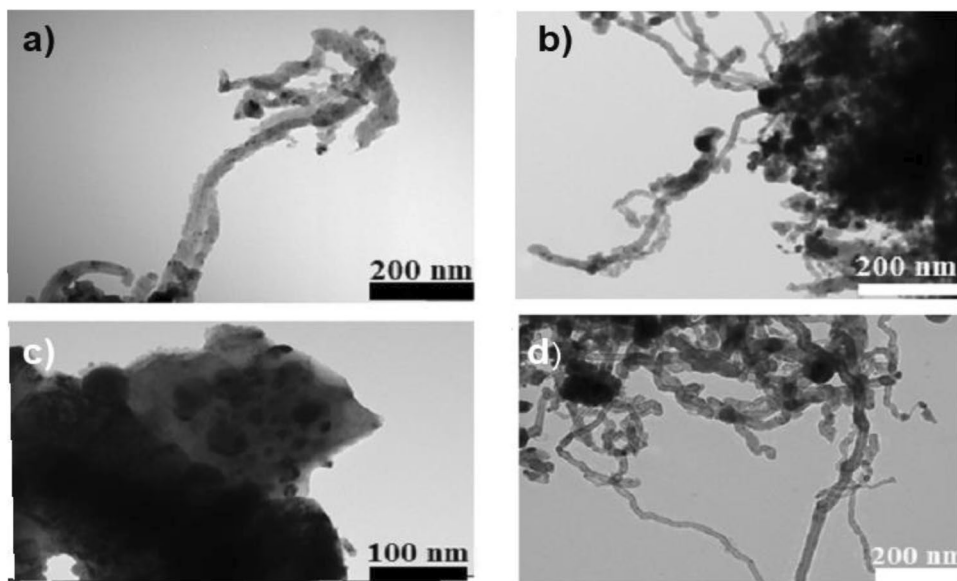


Fig. 9 **a** Rate for methane and CO₂ transformation and carbon balance, **b** space time yields (STY) of H₂ and CO and H₂/CO ratio in DRM over 15Ni-15Mn-20Al for 20 h. Notation: 1. First day, 2. Second day, 3. Third day. Conditions: $V_{\text{cat}}=2$ mL, GHSV = 3000 h⁻¹ at 850 °C

Fig. 10 TEM micrographs of the spent catalysts **a**) 15Ni-15Mn-20Al spent in short-term test; **b**) 15Ni-15Mn-20Al spent in 600–900 °C and back to 600 °C; **c**) 15Ni-35Mn spent in short-term test; **d**) 15Ni-15Mn-20 Mg spent in 600–900 °C and back to 600 °C



particles located on the tip was reported. It is well known, that Ni can be released from the support, when carbon goes through metal. Regarding Ni-Mn catalyst, no carbon nanotubes [47] were observed in Fig. 10c contrary to 15Ni-15Mn-20Al (Fig. 10a). However, the former catalyst possessed a higher deactivation rate than Ni-Mn-Al in short-term stability test (Table 6).

Furthermore, 15Ni-15Mn-20 Mg catalyst used in the temperature cycling experiment, contained large amounts of carbon nanotubes with the maximum diameter of 28 nm (Fig. 10c). This catalyst had more coke after the temperature cycling test than 15Ni-15Mn-20Al based on TPO results (see Section 3.3.5). In comparison with Mn containing catalysts, for 15Ni-35Al [30] and 12 wt.% Ni/ α -Al₂O₃, discussed in the previous study [31], narrower carbon nanotubes were observed.

3.3.2 Porosity and Surface Area

Textural properties of the spent catalysts were determined by nitrogen physisorption demonstrating low surface areas (Table 9). It is noteworthy that the surface area of spent 12 wt.% Ni/ α -Al₂O₃ prepared by the impregnation method was higher [31] in comparison with the spent catalysts containing manganese.

A comparison of the surface areas of the fresh and spent catalysts used in DRM at 850 °C for 30 min revealed, that for 15Ni-35Mn no decline of the surface area was observed (Table 9). For monometallic 12 wt.% Ni/ α -Al₂O₃ catalyst ca. 70% surface area in comparison to the fresh one, was retained. When comparing the total pore volume of the fresh and spent catalysts, it can also be seen, that in some cases, the pore volume increased, for example for 15Ni-35Mn,

most probably due to formation of carbon nanotubes on the external surface of the catalyst.

3.3.3 CHNS Analysis

The carbon content normalized by gram of Ni was quantitatively determined by CHNS analysis for the spent catalysts used in DRM at 850 °C for 30 min (Table 9). A high normalized carbon content was obtained for 15Ni-15Mn-20Al, in which the Ni/Mn molar ratio was 0.8 (Table 1). It was reported in [23], that a low amount of carbon was also observed for a spent Ni-MnO/ γ -Al₂O₃ with the Ni/Mn molar ratio of 0.64 after DRM at 650 °C. It should, however, be kept in mind that the latter result was obtained at temperature much lower than in the current case.

3.3.4 Thermogravimetric Analysis

TGA analysis was performed for the selected catalysts used in short-term DRM experiments at 850 °C for 30 min. According to TGA (Fig. 11), the amount of carbon 15Ni-15Mn-20Al (1.4 wt.%). The same order was observed by CHNS analysis, described above. The peak of the heat release occurring at 575 °C indicates formation of filamentous coke, as observed in Ni catalysts supported on Fe/Mg

waste slug oxides [48] and FeNi/H-Y-5.1 [49]. In addition, it was reported that filamentous carbon can be formed at 450~500 °C [50]. Furthermore, TGA analysis of the fresh catalysts in the presence of either nitrogen or air, revealed phase transformations for 15Ni-15Mn-20Al (5.6 wt.%). A rather high coke formation was also observed in different Mn-Ni-Al₂O₃ catalysts, however, the coke formation can be suppressed by increasing the amount of Mn to an equimolar ratio [32]. It was also stated that Mn with moderate basicity, facilitates CO₂ adsorption even on Ni and can remove carbonaceous species [23]. On the other hand, MnO_x can block Ni sites in Ni/ γ -Al₂O₃ promoted by MnO, increasing catalyst stability [51]. The formation of graphitic coke in 15Ni-35Al was observed at 600 °C [30].

3.3.5 Oxidative Behavior of the Spent Catalysts

Temperature programmed oxidation (TPO) measurements of two spent catalysts used in temperature cycling experiments revealed, that the amount of burnt coke was decreasing in the following order: 15Ni-15Mn-20 Mg (29 wt%) > 15Ni-15Mn-20Al (27 wt.%), when the amounts of CO and CO₂ were calculated as burnt carbon (Fig. 12). The corresponding peak maxima for releasing carbon were 622 °C for 15Ni-15Mn-20 Mg, 559 °C for 15Ni-15Mn-20Al. Regarding

Fig. 11 Influence of temperature on **a)** mass of the catalyst; **b)** heat release during TGA tests for 15Ni-15Mn-20Al catalyst. Temperature was taken as in DRM tests from 100 °C to 800 °C with 10 °C/min in 100 mL/min of gas flow. Legend: fresh catalyst in nitrogen flow (dot-dot line), fresh catalyst in air flow (solid line), spent catalyst in air flow (dash-dash line)

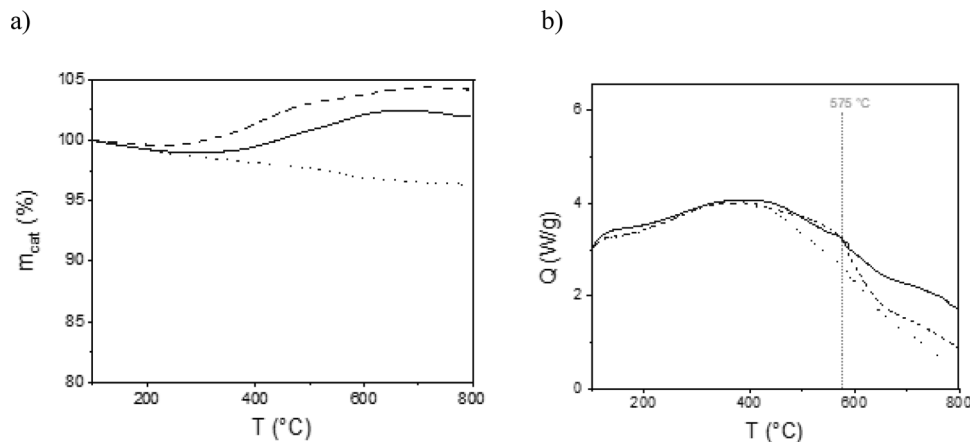
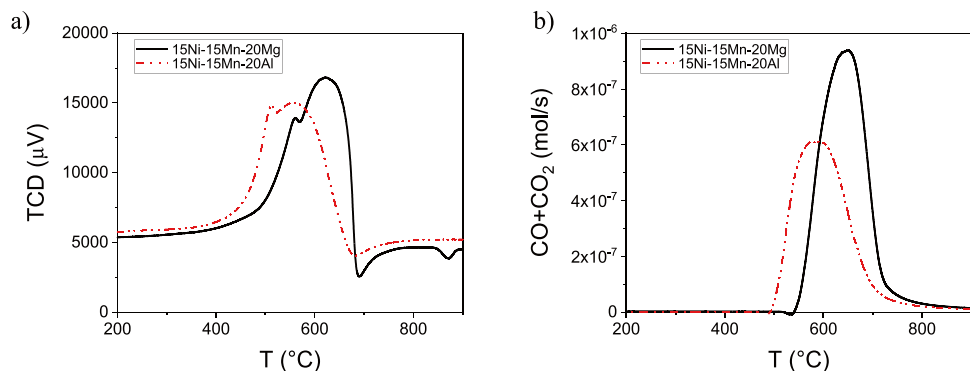


Fig. 12 Influence of temperature on **a)** TPO curves and **b)** quantity of the generated CO and CO₂ for spent 15Ni-15Mn-20 Mg (black), 15Ni-15Mn-20Al (red) catalysts used in the temperature cycling test



TPO analysis, it has been reported in the literature [49], that the peak appearing at 600 °C in TPO corresponds to α -carbon, which is typically formed in the initial stages of reforming [51], while β -carbon appearing at ca. 800 °C is less reactive with CO₂ than α -carbon. In the current case, the results clearly show that 15Ni-15Mn-20 Mg exhibited a more stable, less reactive coke than 15Ni-15Mn-20Al, which is also partially caused by high acidity of the latter catalyst (Table 3).

Typically, the coke can be readily eliminated through oxidation using O₂ [52]. In [53] the Pt-Sn/ γ -Al₂O₃ catalysts experienced coke deposition, when exposed to cyclopentane at 500 °C during cyclohexane dehydrogenation. The coke was subsequently removed either completely or partially by treating the catalysts with O₂ at 450 °C. Thermal programmed oxidation (TPO) analysis revealed, that O₂ effectively combusted the coke, reaching its peak efficiency at 500 °C. In the current work, the coke can be removed by burning with oxygen at 559 – 622 °C. Water is eliminated initially at 300 °C, while above 500 °C, formation of CO and CO₂ takes place.

4 Conclusion

Ni-based bi- and trimetallic catalysts were prepared by the solution combustion synthesis and wet impregnation methods and tested in dry methane reforming (DRM). The influence of Mn and Mg on the physicochemical features of this series of catalysts was analyzed by different characterization techniques. Catalyst activity was tested in temperature cycling DRM at 600–900 °C and back to 600 °C. Furthermore, the stability test of the least coking catalyst was carried out at 850 °C for 20 h.

The nickel particle size was increased after DRM reaction according to TEM analysis. However, with increasing time on stream, metallic nickel was formed during DRM. The Ni-Mn-Mg catalyst in the absence of Al exhibited lower activity in comparison with Ni-Mn-Al. The former catalyst was the most acidic among all catalysts, generating a large amount of coke. As a comparison with the catalysts prepared by the solution combustion method, hydrogen consumption during temperature programmed reduction of Ni/ α -Al₂O₃ was the lowest among all catalysts due to the strong metal-support interactions. The long-term dry methane reforming results showed, however, that both Ni-Mn-Al showed stable space-time yields for hydrogen and CO formation at 850 °C. 15Ni-15Mn-20Al demonstrated good stability without any significant loss in activity for 20 h.

Acknowledgements This research has been funded by the Science Committee of the Ministry of Education and Science of the Republic of Kazakhstan (Grant No. AP14869966).

Funding Open access funding provided by Åbo Akademi University.

Open Access This article is licensed under a Creative Commons Attribution 4.0 International License, which permits use, sharing, adaptation, distribution and reproduction in any medium or format, as long as you give appropriate credit to the original author(s) and the source, provide a link to the Creative Commons licence, and indicate if changes were made. The images or other third party material in this article are included in the article's Creative Commons licence, unless indicated otherwise in a credit line to the material. If material is not included in the article's Creative Commons licence and your intended use is not permitted by statutory regulation or exceeds the permitted use, you will need to obtain permission directly from the copyright holder. To view a copy of this licence, visit <http://creativecommons.org/licenses/by/4.0/>.

References

- Atelge MR, Krisa D, Kumar G, Eskicioglu C, Nguyen DD, Chang SW, Atabani AE, Al-Muhtaseb AH, Unalan S (2020) Waste Biomass Valoriz 11:1019–1040
- Calbry-Muzyka A, Madi H, Rüsche-Pfund F, Gandiglio M, Biollaz S (2022) Renew Energy 181:1000–1007
- Jang WJ, Shim JO, Kim HM, Yoo SY, Roh HS (2019) Catal Today 324:15–26
- Gašparič L, Pintar A, Kokalj A (2024) Appl Surf Sci 648:159029
- Thi Bach MH, Tran NT, Thi Tran TN, Nguyen VC, Thi Nguyen HA (2021) Alumina support for cobalt catalyst in a methane dry reforming reaction: the role of water content in a solvent medium. Int J Chem Eng 6681796:1–9
- Zhang F, Liu Z, Chen X, Rui N, Betancourt LE, Lin L, Xu W, Sun CJ, Abeykoon AMM, Rodriguez JA, Teržan J, Lorber K, Djinović P, Senanayake SD (2020) ACS Catal 10:3274–3284
- Jin B, Li S, Liang X (2021) Fuel 284:119082–119090
- Littlewood P, Xie X, Bernicke M, Thomas A, Schomäcker R (2015) Catal Today 242:111–118
- Ray D, Reddy PMK, Subrahmanyam C (2018) Catal Today 309:212–218
- Luna AEC, Iriarte ME (2008) Appl Catal A: Gen 343:10–15
- Choi JS, Moon KI, Kim YG, Lee JS, Kim CH, Trimm DL (1998) Catal Lett 52:43–47
- Gili A, Schlicker L, Bekheet MF, Görke O, Penner S, Grünbacher M, Götsch T, Littlewood P, Marks TJ, Stair PC, Schomäcker R, Doran A, Selve S, Simon U, Gurlo AA (2018) ACS Catal 8:8739–8750
- Yao L, Galvez ME, Hu C, Da Costa P (2018) Ind Eng Chem Res 57:16645–16656
- Degen T, Sadki M, Bron E, König U, Nénert G (2014) Powder Diffr 29: Supplement S2:S13–S18
- Gates-Rector S, Blanton T (2019) Powder Diffr 34:352–360
- Ferrandon MS, Byron C, Celik G, Zhang Y, Ni C, Sloppy J, McCormick RA, Booksh K, Teplyakov AV, Delferro M (2022) Appl Catal A: Gen 629:118379–118393
- Murzin DYu (2022) 2nd Ed De Gruyter, Berlin
- Jović VD, Maksimović VM, Pavlović GK, Popov I (2006) J Solid State Electrochem 10:373–379
- Tang G, Gong D, Liu H, Wang L (2019) Catalysts 9:442–453
- Netskina OV, Dmitruk KA, Paletsky AA, Mukha SA, Pochtar AA, Bulavchenko OA, Prosvirin IP, Shmakov AG, Ozerova AM, Veselovskaya JV, Mazina OI, Komova OV (2022) Catalysts 12:1274–1294
- Saputra E, Muhammad S, Sun H, Ang HM, Tadé MO, Wang S (2013) Appl Catal B: Environ 142–143:729–735
- Padmapriya G, Sivachandiran M (2020) Malaya J Matem S:1081–1083

23. Seok SH, Hwan SH, Lee JS (2001) *Appl Catal A: Gen* 215:31–38
24. Dankwah JR, Koshy P (2014) *High Temp Mater Processes (London)* 33:345–353
25. Danghyan V, Kumar A, Mukasyan A, Wolf EE (2020) *Appl Catal B: Environ* 273:119056
26. Wang Y, Li B, Xiao YS, Liu ZW (2023) *Processes* 11:596
27. Kurmashov P, Ukhina I, Manahov A, Ishchenko AV (2023) *Appl Sci* 13:3962–3974
28. Alvarez-Galvan C, Falcon H, Cascos V, Troncoso L, Perez-Ferreas S, Capel-Sanchez M, Campos-Martin JM, Alonso JA, Fierro JLG (2018) *Int J Hydrogen Energy* 43:16834–16845
29. Abu-Zied B, Asiri AM (2012) *J Nanomat* 1–7
30. Manabayeva AM, Mäki-Arvela P, Vajglová Z, Martínéz-Klimov M, Tirri T, Baizhumanova TS, Grigor'eva VP, Zhumabek M, Aubakirov YA, Simakova IL, Murzin DYU, Tungatarova SA (2023) *Ind Eng Chem Res* 62:11439–11455
31. Manabayeva AM, Mäki-Arvela P, Vajglová Z, Martínéz-Klimov M, Yevdokimova O, Peuronen A, Lastusaari M, Tirri T, Kassymkan K, Baizhumanova TS, Zhumabek M, Sarsenova RN, Zheksenbaeva ZT, Murzin DYU, Tungatarova SA (2023) *Ind Eng Chem Res* 62:20588–20607
32. Franz R, Pinto D, Uslamin EA, Urakawa A, Pidko EA (2021) *ChemCatChem* 13:5034–5046
33. Xu HL, Shen W, Yang YT (2001) *Chin J Chem* 19:647–651
34. Tamimi K, Alavi SM, Rezaei M, Akbari E (2021) *J Energy Inst* 99:48–58
35. Kim SC, Park YK, Nah JW (2014) *Powder Technol* 266:292–298
36. Zhang Y, Qin Z, Wang G, Zhu H, Dong M, Li S, Wu Z, Li Z, Wu Z, Zhang J, Hu T, Fan W, Wang J (2013) *Appl Catal B* 129:172–181
37. Suo C, Liu Y, Zhang X, Wang H, Chen B, Fang J, Zhang Z, Chen R, Chen R, Shi C (2022) *Eur J Inorg Chem* 23:e202200182
38. Zhan Y, Song K, Shi Z, Wan C, Pan J, Li D, Au C, Jiang L (2019) *Int J Hydrog Energy* 45:2794–2807
39. Gao X, Ge Z, Zhu G, Wang Z, Ashok J, Kawi S (2021) *Catalysts* 11:1003–1021
40. Seok SH, Choi SH, Park ED, Han SH, Lee JS (2002) *J Catal* 209:6–15
41. Choya A, de Rivas B, No ML, Gutiérrez-Ortiz JI, López-Fonseca R (2024) *Fuel* 358:130166
42. Liu H, Hadjitaief HB, Benzina M, Gálvez ME, Da Costa P (2019) *Int J Hydrog Energy* 44:246–255
43. Yao L, Zhu J, Peng X, Tong D, Hu C (2013) *J Hydrog Energy* 38:7268–7279
44. Lanre MS, Abasaeed AE, Fakeeha AH, Ibrahim AA, Al-Awadi AS, Jumah AB, Al-Mubaddel FS, Al-Fatesh AS (2022) *Catalysts* 12:715
45. Arbag H, Yasyerli S, Yasyerli N, Dogu T, Dogu G (2013) *Top Catal* 56:1695–1707
46. Zhou L, Li L, Wei N, Li J, Basset JM (2015) *ChemCatChem* 7:2508–2516
47. Najfach AJ, Almquist CB, Edelmann RE (2021) *Catal Today* 369:31–47
48. Sahraei OA, Desgagnés A, Larachi F, Iliuta MC (2020) *Appl Catal B-Env* 279:119330
49. Vajglová Z, Gauli B, Mäki-Arvela P, Simakova IL, Kumar N, Eränen K, Tirri T, Lassfolk R, Peurla M, Doronkin DE, Murzin DY (2023) *J Catal* 421:101–116
50. Yuan B, Zhu T, Han Y, Zhang X, Wang M, Li C (2023) *Atmosphere* 14:770
51. Nagaoka K, Seshan K, Aika KI, Lercher JA (2001) *J Catal* 197:34–42
52. Zhou J, Zhao J, Zhang J, Zhang T, Ye M, Liu Z (2020) *J Catal* 41:1048–1061
53. Pieck CL, Vera CR, Querini CA, Parera JM (2005) *Appl Catal A: Gen* 278:173–180

Publisher's Note Springer Nature remains neutral with regard to jurisdictional claims in published maps and institutional affiliations.